CrossMark

Study on the zinc doping and annealing effects of sprayed In$_2$O$_3$ thin films

Nasreddine Beji[1] · Mehdi Souli[1] · Sonia Azzaza[2] · Safia Alleg[2] · Najoua Kamoun Turki[1]

Abstract Zinc doped indium oxide thin films (In$_2$O$_3$:Zn) have been successfully prepared on glass substrates using spray pyrolysis technique for different zinc concentrations y $\left(y = \frac{[Zn^{2+}]}{[In^{3+}]} = 0, 1, 2, 3, 4, 5 \text{ and } 6 \text{ at.}\%\right)$. The structure, surface morphology, optical and electrical properties of In$_2$O$_3$:Zn thin films were investigated by X-ray diffraction, atomic force microscopy, spectrophotometer, fluorescence spectrometer and Hall Effect. It is found that physical properties of In$_2$O$_3$ material are affected by doping with zinc element. Structural analysis shows that In$_2$O$_3$ thin layers are polycrystalline with cubic structure. After doping, a double transition of preferential orientation was observed from (222) to (400) for y = 1 at.% and from (400) to (440) for y = 3 at.%. The best crystallinity is obtained for y = 1 at.% with (400) as a preferred orientation. The maximum grain size is obtained for y equals to 1 at.%. Optical transmission shows an average value after doping of about 80 % with interference fringes revealing the good uniformity and homogeneity of deposited layers. After doping, the direct band gap E$_g$ is equals to 3.51 eV for In$_2$O$_3$:Zn (1 at.%). The single oscillator energy E$_0$ and dispersion energy E$_d$ were determined by Wemple model using the envelope method. We obtained E$_0$ = 2 × E$_g$ for doped films. Electrical resistivity (ρ) decreases from 650.20 × 10^{-3} to 198.50 × 10^{-3} Ω cm for respectively undoped and In$_2$O$_3$:Zn (1 at.%). A heat treatment under nitrogen atmosphere of In$_2$O$_3$:Zn (1 at.%) thin films leads to enhanced optical transmission especially for 250 (2 h) and 450 °C (2 h). A significant decrease of the resistivity to about 2.82 × 10^{-3} Ω cm is obtained for annealing temperature equals to 250 °C (2 h). All these experimental results lead to consider that annealed zinc doped indium oxide thin films can be used as transparent conductive oxide material in optoelectronic applications.

1 Introduction

Recently, transparent conductive oxides (TCO) materials have been investigated for their potential applications in different domains. Among these materials, indium oxide thin films have attracted more interest thanks to their promising properties like high transparency, wide band gap and low electrical resistivity [1]. Indium oxide thin films have been used in optoelectronic devices [2] such us photovoltaic devices [3], thin films transistor [4], light emitting diodes [5] and in gas sensing applications [6, 7]. In$_2$O$_3$ thin films can be grown using various deposition techniques like spray pyrolysis [6, 8], sol gel [9], magnetron sputtering [10] and laser ablation [11]. In the present work, we have synthesized zinc doped indium oxide thin films by spray pyrolysis technique. In our knowledge, only a report [12] has investigated about physical properties of In$_2$O$_3$:Zn thin films grown by spray. In fact, Jothibas et al. [12] have used quite different experimental conditions compared to us which have produced naturally other experimental results that enrich and enhance research studies about this material. In our case, In$_2$O$_3$:Zn have been synthesized with different doping concentration (0, 1, 2, 3,

✉ Nasreddine Beji
  beji.nasreddine@gmail.com

1 LR99ES13 Laboratoire de Physique de la Matière Condensée (LPMC), Département de Physique, Faculté des Sciences de Tunis, Université Tunis El Manar, 2092 Tunis, Tunisia

2 Laboratoire de Magnétisme et Spectroscopie des Solides (LM2S), Département de Physique, Faculté des Sciences, Université Badji Mokhtar Annaba, B.P. 12, 23000 Annaba, Algeria

🌱 Springer

4, 5 and 6 at.%) using other chemical precursors indium chloride ($InCl_3$) and Zinc acetate dehydrate ($Zn(CH_3COO)_2 \cdot 2H_2O$)) and thin film deposition was carried out at a different substrate temperature ($T_s = 500\ °C$). Besides, the solution flow rate and the distance nozzle—sample used in our study are different to those chosen elsewhere [12]. In this paper, we have studied structural, optical and electrical properties of zinc doped indium oxide thin films. Elaborated thin layers were characterized using X-ray diffraction, atomic force microscopy (AFM), spectrophotometers, fluorescence spectrometer and Hall Effect. To analyze deeply structural properties of deposited layers, the XRD patterns were refined using the MAUD program [13] which has not been done previously for In_2O_3:Zn. Moreover, the single oscillator energy E_0 and dispersion energy E_d were determined using Wemple oscillatory model for all doped films. Finally, a heat treatment was performed to enhance optical and electrical properties of zinc doped indium oxide thin films which, in our knowledge, has not done before for In_2O_3:Zn elaborated by spray.

2 Experimental setup

Zinc doped indium oxide thin films were grown by the pulverization technique in liquid phase (spray). Indium chloride ($InCl_3$) dissolved in bi-distilled water was used to grow undoped indium oxide. Zinc acetate dehydrate ($Zn(CH_3COO)_2 \cdot 2H_2O$) was added to the initial solution to provide zinc doping element. In_2O_3:Zn thin films were deposited on heated glass substrates at 500 °C. Compressed air was used as a carrier gas. The solution flow rate is fixed to 2.5 ml min^{-1}. The distance nozzle—sample is 28 cm. The experimental setup of spray growth was described and detailed in a previous work [14]. Atomic concentrations of zinc in the solution $y = \left(\frac{[Zn^{2+}]}{[In^{3+}]}\right)_{sol}$ were 0, 1, 2, 3, 4, 5 and 6 at.%. Structural properties were investigated using X-ray diffraction (XRD) which are recorded with an automated Bruker D8 advance X-Ray diffractometer with CuK_α radiation ($\lambda_{Cu} = 1.5418\ Å$) for 2θ values in the range of 10°–80°. The wavelength, accelerating voltage and current were respectively, 1.5418 Å, 40 kV and 20 mA. Film surface morphology was studied by atomic force microscopy (AFM, standard Veeco Dimension 3100, used in tapping mode). Optical transmission and reflection measurements were examined with Perkin-Elmer Lambda 950 spectrophotometer in the wavelength range of 250–2500 nm at room temperature taking air as reference. Photoluminescence (PL) was studied with Perkin-Elmer LS 55 Fluorescence spectrometer using 375 nm as an excitation wavelength. Electrical resistivity, volume carrier concentration and mobility were

determined by Hall Effect in the Van der Pauw configuration. Heat treatment process was performed using a Jet First Processor™. XRD patterns of zinc doped In_2O_3 thin films were also refined by the MAUD software [13] which is based on the Rietveld method [13]. In order to reduce the difference between experimental and theoretical diffraction patterns, the fitting procedure is controlled by the Marquardt least square method [13].

3 Results and discussion

3.1 Structural properties

3.1.1 XRD Analysis

XRD patterns of zinc doped indium oxide thin films for different zinc concentrations are shown in Fig. 1. The diffraction peaks are very narrow indicating the good crystallinity of deposited films. All films crystallize into body centered cubic structure (JCPDS Card no. 06-0416).
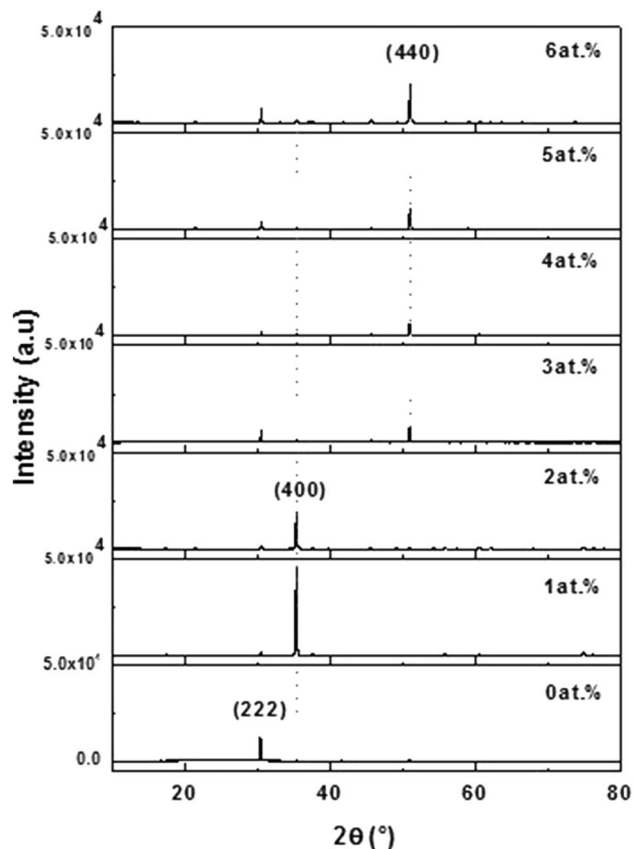

Fig. 1 XRD patterns of undoped and zinc doped In_2O_3 thin films for different zinc concentration y in the spray solution $\left[y = \left(\frac{[Zn^{2+}]}{[In^{3+}]}\right)_{sol} = 0, 1, 2, 3, 4, 5$ and $6\,at.\%\right]$

XRD observations reveal that undoped films have a preferred orientation along (222) plan for $2\theta = 30.58°$. After doping, a double transition of preferential orientation was observed from (222) to (400) for y = 1 at.% and from (400) to (440) for y = 3 at.%. It is inferred from such observation that change in the preferred orientation strongly depends on incorporation of zinc in the crystal lattice. In fact, for increasing zinc concentration in the sprayed solution, the doping atoms do not occupy proper sites in In_2O_3 lattice [15]. Similar results have been reported for molybdenum doped indium oxide thin films [15–17]. The different papers suggest that doping atoms placed at regular as well as interstitial sites do not lead to a change of the preferred orientation. Nevertheless, the occupancy of doping atoms on additional interstitial sites which are unoccupied previously leads to a change in the preferred orientation [15]. In our case, for y = 1 at.%, the zinc atoms can be incorporated at additional interstitial sites [15–17] and/or additional vacancy sites [8] which are unoccupied previously leading to the change of the preferred orientation from (222) to (400). Indeed, In_2O_3 thin layers have several types of defects levels like indium and oxygen vacancies and indium interstitial sites [18]. In_2O_3 thin films grown for y = 1 at.% exhibit the highest intensity of the preferred orientation which correspond to a better crystalline quality compared to all other films. For increasing zinc concentration beyond 2 at.%, the excess inclusion of even host cation may be lead to the change of the preferred orientation peak from (400) to (440). Indeed, zinc elements may occupy either type of additional sites. As a conclusion, it can be summarized that the doping ratio in the sprayed solution influence the cristallinity of the zinc doped In_2O_3 thin film. For higher doping, there is a noticeable degradation of the thin film's cristallinity with increasing amounts of zinc. The change in the preferred orientation can be also associated with AFM images. Indeed, it can be observed from Fig. 5 that the development of microstructure which is controlled by the doping ratio is related to the change in the preferred orientation.

We note also the appearance of secondary phase of ZnO due to the doping process. Indeed, the presence of (100) diffraction peak (Fig. 2) is located at 31.88° corresponds to the hexagonal ZnO phase (JCPDS Card n°89-1397). These experimental results are in good agreement with those observed elsewhere [12] at higher zinc doping concentration (11 at.%) along (100) and (102) plans related to the ZnO phase.

3.2 Rietveld analysis

XRD spectra of zinc doped In_2O_3 thin films were fitted by MAUD software [13] which is based on Rietvled method [13]. Figure 3 shows the Rietveld refinements of XRD pattern for In_2O_3:Zn (1 at.%). The structural parameters (lattice parameters, microstrain, crystallite sizes and phases amounts) given by fitting process are summarized in Table 1. The Rietveld refinement reveals the presence of In_2O_3 and ZnO phase. The relative proportion of the zinc oxide phase increases when zinc concentration increases and reaches a maximum value of 12.7 % for 6 at.% (Table 1). The lattice parameter (a) of the cubic centered In_2O_3 thin layers is in the order of 10.1280 and 10.1221 Å for respectively undoped and In_2O_3:Zn (1 at.%). Furthermore, the lattice parameter (a) of the indium oxide In_2O_3 increases with zinc content and attains a maximum value of 10.1308 Å for 6 at.% zinc concentration. Up to y equals to 2 at.%, the crystal lattice is contracted after doping. However, beyond 3 at.% we note an expansion of the crystal lattice compared to the undoped ones. The increase of the microstrain $<\sigma^2>^{1/2}$ after doping may be caused by the incorporation of zinc atoms in the In_2O_3 crystal lattice. Figure 4 exhibits the variation of the average grain size $<d>$ of zinc doped In_2O_3 thin films calculated by MAUD software as a function of doping concentration y. A maximum value of about 93.4 nm is obtained for y = 1 at.%. This result is in good agreement with the fact that In_2O_3:Zn (1 at.%) thin layers have the best crystallinity as found in XRD analysis. In fact, for this doping level the preferred orientation exhibits the highest intensity compared to all other films (Fig. 1) which leads to a minimum of structural defects and reduce of grain boundaries. So, such result indicates that the concentration of Zn^{2+} affects the crystal growth direction and assists the grain growth up to the optimum concentration equal to 1 at.% with a minimum of structural defects. This indicates that a low zinc concentration promotes the formation of In_2O_3 grains accelerating the nucleation rate and allowing the particle to grow larger
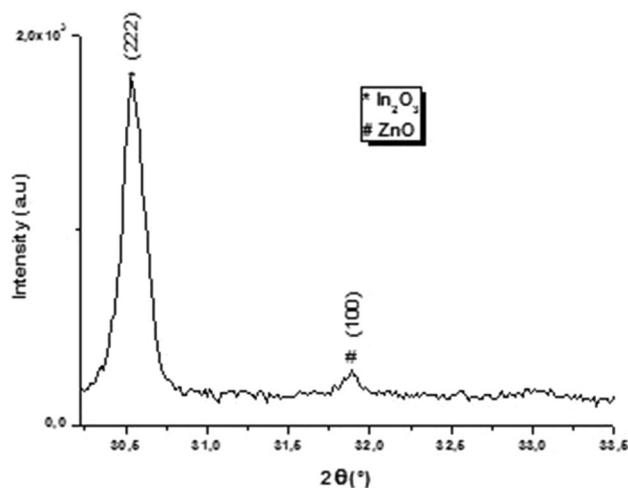

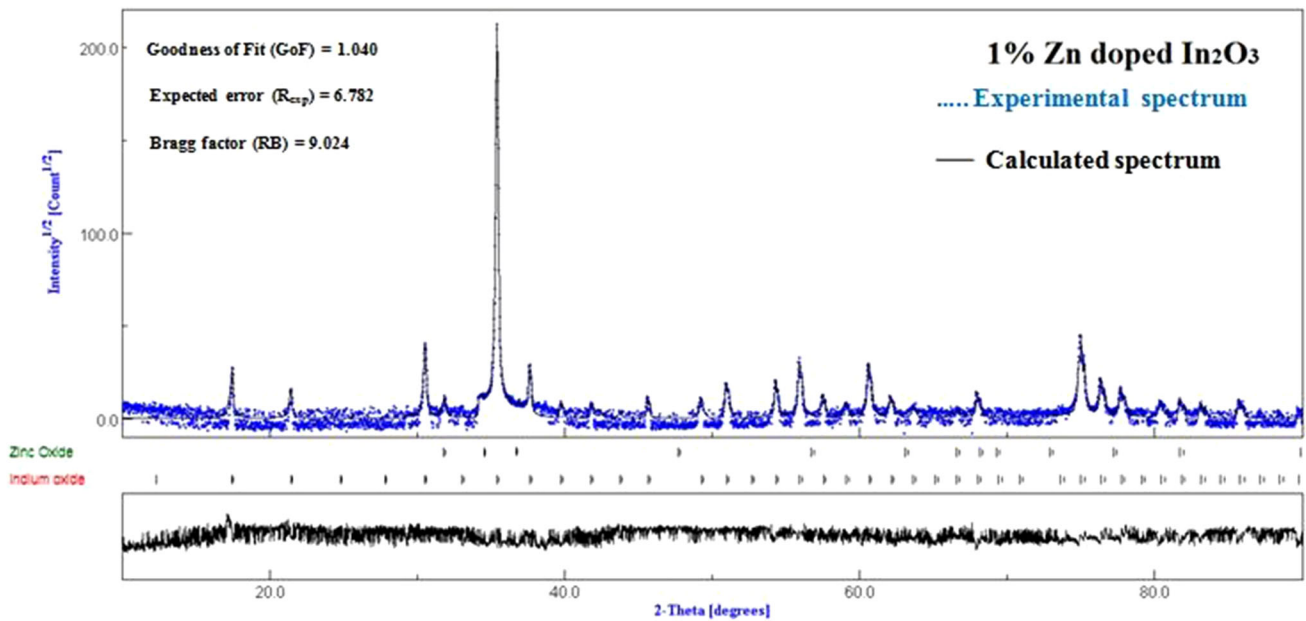Fig. 2 Zoom of XRD spectrum for zinc concentration y equals to 1 at.%

Fig. 3 Rietveld refinement of XRD spectrum of zinc doped indium oxide thin films for y = 1 at.%. The difference between the experimental (*dots*) and the calculated (*full line*) spectrum is given below

Table 1 Phases and microstructure parameters determined by MAUD software for zinc doped In_2O_3 thin films $\left[y = \left(\frac{[Zn^{2+}]}{[In^{3+}]}\right)_{sol} = 0, 1, 2, 3, 4, 5 \text{ and } 6 \text{ at.\%}\right]$

y (at.%)	Phases	Microstructure $<\sigma^2>^{1/2}$ (%) (±0.002)	Lattice parameters (Å) (±0.0001)		Amount (%) (±0.4)
			a	c	
0	**In_2O_3**	**0.0208**	**10.1280**	**/**	**100**
1	**In_2O_3**	**0.041**	**10.1221**	**/**	**96.25**
	ZnO	0.030	3.2417	5.1876	3.75
2	**In_2O_3**	**0.054**	**10.1231**	**/**	**95.12**
	ZnO	0.041	3.2393	5.1872	4.88
3	**In_2O_3**	**0.051**	**10.1287**	**/**	**94.7**
	ZnO	0.028	3.2385	5.1866	5.3
4	**In_2O_3**	**0.060**	**10.1303**	**/**	**92.45**
	ZnO	0.032	3.2317	5.1757	7.55
5	**In_2O_3**	**0.052**	**10.1305**	**/**	**90.2**
	ZnO	0.024	3.2313	5.1760	9.8
6	**In_2O_3**	**0.031**	**10.1308**	**/**	**87.3**
	ZnO	0.026	3.2309	5.1759	12.7

Distinguish between the In_2O_3 and ZnO phases are highlighted in bold

[19]. Further, the direction of preferred peak can be shifted between the planes by varying the Zn doping ratio.

3.3 Morphological properties

Atomic force microscopy (AFM) images for undoped and zinc doped In_2O_3 thin films are presented in Fig. 5. It is noted an increase of the grain size for y = 1 at.% compared to the undoped one. This is in good accordance with the results obtained from the Rietveld refinements of the XRD patterns.

When zinc concentration is increasing from 0 to 2 at.%, a clear change of grain form is observed. From y equal to 3 at.%, the micrographs reveal the presence of grains with different form and size in different spatial distribution. This last result may be attributed to the change of predominant peak when y increases. The incorporation of zinc element and the variation of doping concentration affect extremely the surface morphology of elaborated films.

RMS roughness values were determined using AFM images. All results are shown in Fig. 6. It is found that
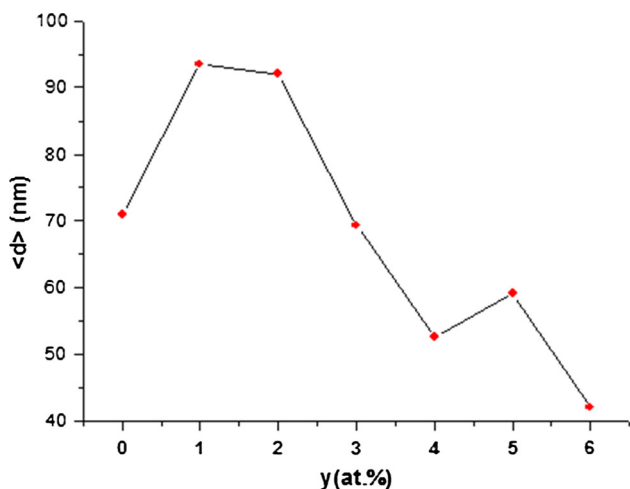
Fig. 4 Average grain size <d> of zinc doped In_2O_3 thin films for different concentrations $\left[y = \left(\frac{[Zn^{2+}]}{[In^{3+}]} \right)_{sol} = 0, 1, 2, 3, 4, 5 \text{ and } 6 \text{ at.}\% \right]$

RMS roughness increases from 48 to 59 nm for respectively undoped and In_2O_3:Zn (1 at.%). The expansion of RMS values can be related to an enhancement of crystallite size as remarked by Liu et al. [20]. Beyond the level of 1 at.% doping, a decrease trend of RMS values is observed. In fact, some authors [9] have reported that the agglomeration can induces a modification in RMS roughness values.

3.4 Optical properties

The optical transmission and reflection spectra of zinc doped indium oxide thin films for different doping concentration y (y = 0, 1, 2, 3, 4, 5 and 6 at.%) are shown Fig. 7. We note the presence of interference fringes in the transparency zone which are characteristics of uniform thickness and homogenous surface layers. This phenomenon is a consequence of interference of incident light beams at the interface between deposited layers and microscope slide substrate [21]. After doping, the transmission (T) decreases slightly but remains still high in the visible and infrared regions except for y = 5 at.%. Indeed, the average transmission was around 80 % for y equals to 1 at.% which corresponds to the best transmission of In_2-O_3:Zn. Our results in terms of film transparency are promising and seem to be better than those reported in other works [6, 12]. Indeed, some reports have found that doping atoms leads to a poor transmission. Pramod et al. [6] have investigated the effect of lithium doping on physical properties of In_2O_3 thin films used as gas sensors. They revealed that the transmission was drastically decreased after doping. Further, Jothibas et al. [12] have reported that zinc doped indium thin layers exhibit a poor percentage of transmission for higher doping level with the absence of interference fringes. The reduction of transmission after doping can be due to the enhanced scattering of photons caused by crystal defects produced by doping or to the absorption of photons by free carriers [12].

The band gap energy E_g is calculated according to the Tauc equation [22]:

$$(\alpha h v) = A \left(h v - E_g \right)^n \tag{1}$$

where (hv) is the photon energy, h is planck's constant, n is equal to (½) for direct band gap, A is a constant and α is the absorption coefficient which can be calculated using the following formula [23]:

$$\alpha = -\frac{1}{t} Ln \left[\frac{T}{(1-R)^2} \right] \tag{2}$$

where t, T and R are respectively the film thickness, transmission and reflection.

The band gap values of zinc doped indium oxide thin films are presented in Fig. 8. The straight line of layers over the wide range of photon energy (hv) confirms the direct transition type. The direct band gap energy was determined by extrapolating the linear part of Tauc plot curves to intercept the energy axis (at αhv = 0). One observes that the band gap energy is in the range of [3.45–3.51] eV for y between 0 and 4 at.%. However from 5 at.%, E_g decreases slightly reaching 3.32 eV for y = 6 at.%. Our obtained results are in agreement with those reported by Jothibas et al. [12]. They found that band gap energy is in the range of [3.28–3.61] eV. The decrease of the band gap for y = 5 and 6 at.% may be due to the zinc elements positioned in donor level. The high doping concentration can reduce the difference between donor level and conduction band which leads to decrease of optical band gap energy [24].

Oscillatory Wemple model have been applied to zinc doped indium oxide thin films. This model suggests that the refractive index (n) can be expressed as a function of photon energy (hv) according to [25]:

$$n^2 - 1 = \frac{E_d E_0}{E_0^2 - (h v)^2} \tag{3}$$

where E_0 is the oscillator energy and E_d is the dispersion energy.

The linear variations of $(n^2 - 1)^{-1}$ versus $(h v)^2$ for zinc doped indium oxide thin films (Fig. 9) permit us to determine E_0 and E_d from the slope $(E_d E_0)^{-1}$ and the intercept at the origin (E_0/E_d) for each straight line. The average
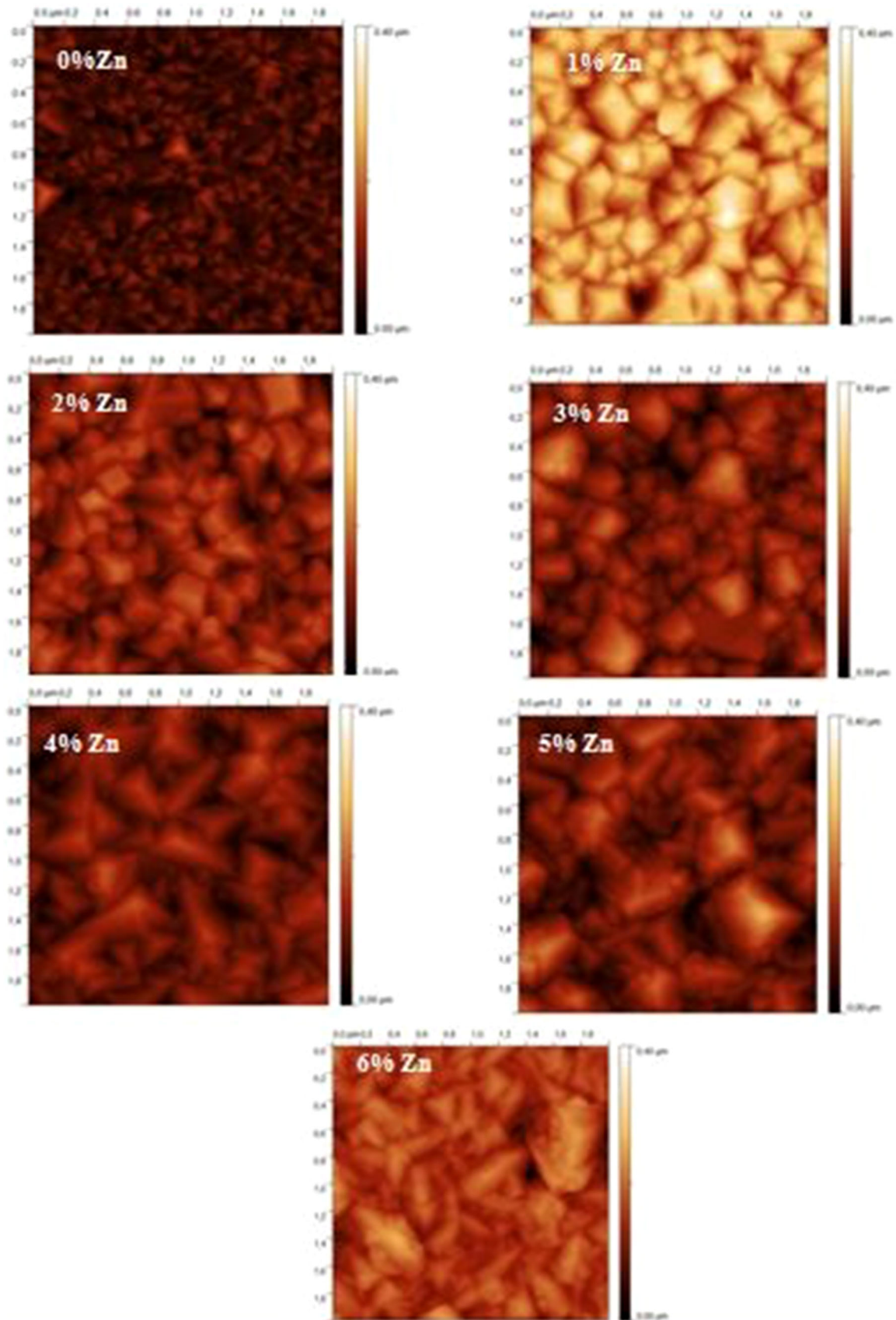
Fig. 5 AFM images of undoped and zinc doped In$_2$O$_3$ thin films for different zinc concentrations in the spray solution $\left[y = \left(\frac{[Zn^{2+}]}{[In^{3+}]} \right)_{sol} = \right.$ 0, 1, 2, 3, 4, 5 and 6 at.%$\left.\right]$
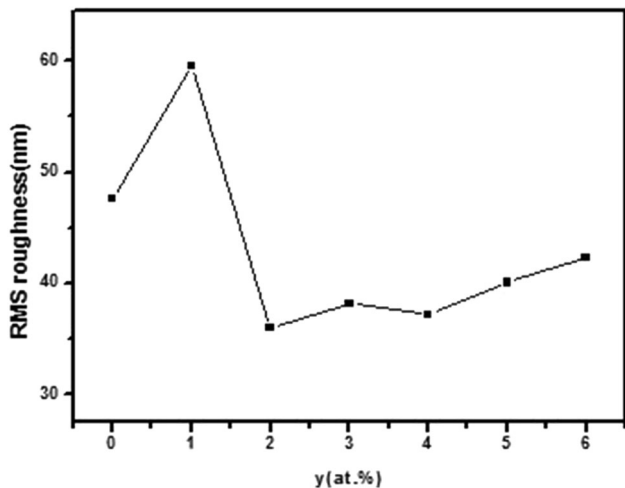

Fig. 6 Variation of the RMS roughness of sprayed zinc doped indium oxide thin films as a function of zinc content $\left[y = \left(\frac{[Zn^{2+}]}{[In^{3+}]} \right)_{sol} = 0, 1, \right.$ 2, 3, 4, 5 and 6 at.%$\left.\right]$

strength S_0 and the wavelength λ_0 of the oscillator are deduced from the Wemple equation as:

$$\lambda_0 = \frac{hc}{E_0} \tag{4}$$

$$S_0 = \frac{E_0 E_d}{(hc)^2} \tag{5}$$

Fig. 8 $(\alpha h\nu)^2$ versus $(h\nu)$ of zinc doped In$_2$O$_3$ thin films for different concentrations $\left[y = \left(\frac{[Zn^{2+}]}{[In^{3+}]} \right)_{sol} = 0, 1, 2, 3, 4, 5 \text{ and } 6 \text{ at.%} \right]$
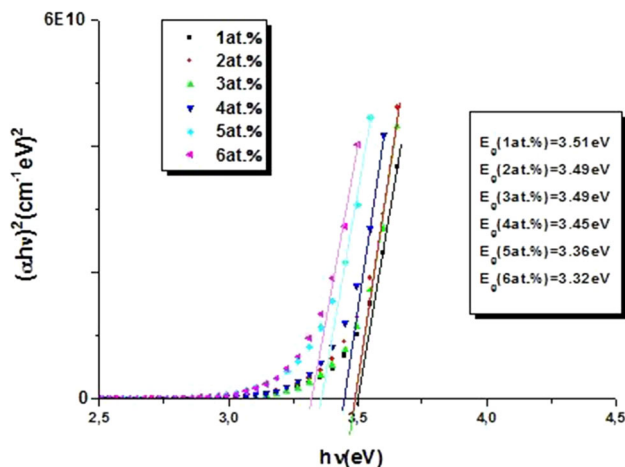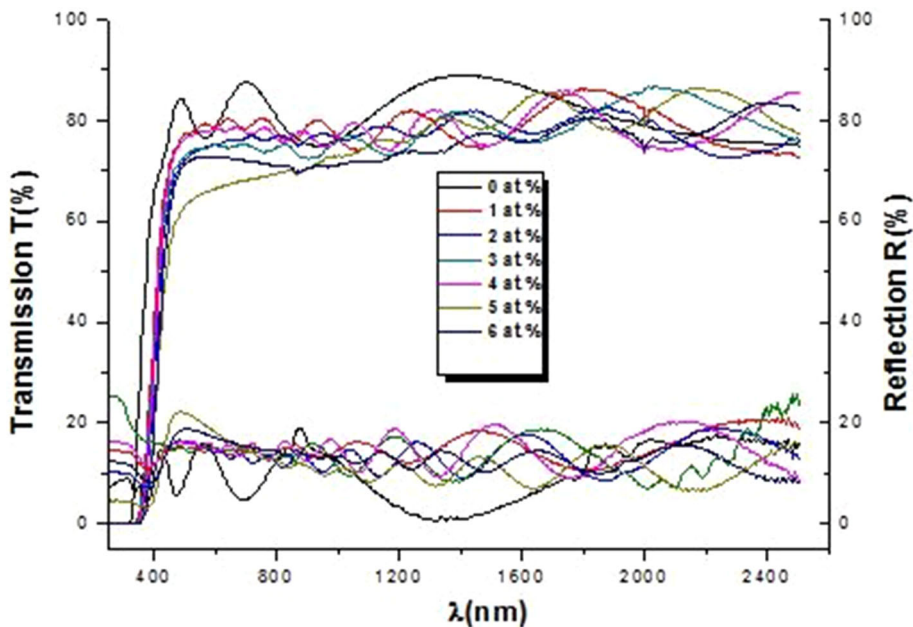
All values of E_0, E_d, S_0 and λ_0, for zinc doped indium oxide thin films, are presented in Table 2. It is seen that the oscillator energy (E_0) is the double of the optical band gap (E_g) for all zinc doped indium oxide thin films. However $E_0 = 1.5 \times E_g$ for undoped In$_2$O$_3$ thin films [8]. This difference in the oscillator energy E_0 may be caused by the incorporation of doping element in the crystal lattice.

3.5 Photoluminescence analysis

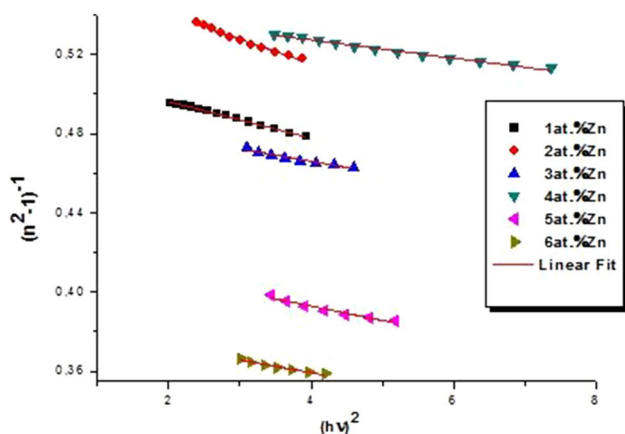Photoluminescence (PL) is a susceptible technique for the characterization of crystal structure or defect levels.

Fig. 7 Optical transmission and reflection spectra of undoped and zinc doped In$_2$O$_3$ thin films for different doping concentrations y $\left[y = \left(\frac{[Zn^{2+}]}{[In^{3+}]} \right)_{sol} = \right.$ 0, 1, 2, 3, 4, 5 and 6 at.%$\left.\right]$

Fig. 9 Plot of $(n^2 - 1)^{-1}$ as a function of $(h\nu)^2$ of zinc doped In_2O_3 thin films for different ratios $\left[y = \left(\frac{[Zn^{2+}]}{[In^{3+}]} \right)_{sol} = 0, 1, 2, 3, 4, 5 \text{ and } 6 \text{ at.}\% \right]$

Generally, the fluorescence of In_2O_3 compound is due to the presence of traps in indium oxide thin films. It is well known that In_2O_3 thin films have several types of defects levels such as indium interstitial, oxygen and indium vacancies [18]. Jothibas et al. [12] have revealed that n-type In_2O_3 with bcc structure exhibits oxygen vacancies leading to the creation of new energy levels in the band gap. Figure 10 shows PL spectra of In_2O_3:Zn thin layers for different doping concentrations y. We note the presence of three principal emission peaks detected at 485, 505 and 795 nm corresponding to energy levels equal respectively to 2.56, 2.45 and 1.55 eV. These PL emissions may be related to lattice defects or oxygen deficiencies in the indium oxide thin films as explained by Kaleemulla et al. [26]. In fact, they have reported that PL process can be produced as follow: electrons located in donor level can be attracted by a hole positioned in acceptor level. So a trapped exciton is formed leading to produce PL emission [26]. A similar emission band is detected in previous work for iron doped indium oxide thin films elaborated by spray [8]. Wu et al. [27] have reported that emission peaks observed in the visible range may be attributed to the

recombination of carrier concentration that occurs between valence band and oxygen vacancies acting as donor levels. Further, the authors have revealed that the difference in PL peaks positions between reports may be related to the morphologies differences as shown in [27].

3.6 Electrical properties

The electrical parameters of undoped and zinc doped In_2O_3 thin films determined from the Hall Effect measurements are listed in Table 3. It is noted an initial decrease of the electrical resistivity (ρ) from 650.20×10^{-3} to 198.50×10^{-3} Ω cm for respectively undoped and In_2O_3:Zn (1 at.%). This result is in accordance with the fact that In_2O_3:Zn (1 at.%) has the best crystallinity. Such decrease in ρ can be attributed to the enlargement of grain size due to the enhancement of the crystal quality as mentioned in the structural section. At this doping level (y = 1 at.%), one notes an increase of Hall mobility from 1.17 to 6.70 cm^2/Vs. Except for y equals to 3 and 6 at.%, volume carrier concentrations (N_v) decreases slightly as a function of doping concentration y but it keep the same order of magnitude (about 10^{18} cm^{-3}).

Beyond y equals to 1 at.%, an increase of the electrical resistivity by an order of magnitude was noted. Such result by me attributed to the increase of crystal defaults and deterioration of crystallinity beyond 1 at.%.

3.7 Annealing effect on the optical and electrical properties of In_2O_3:Zn (1 at.%)

In order to ameliorate thin films transparency, In_2O_3:Zn (1 at.%) were heated. The annealing was carried out in nitrogen atmosphere at 250 and 450 °C for 1 and 2 h. Figure 11 shows transmission spectra of as deposited and annealed In_2O_3 films for y = 1 at.%. After annealing, all films have interferences fringes in the transparency zone. An increase of the transmission in the visible region is observed for 250 (2 h) and 450 °C (2 h). It can be seen that transmission was enhanced for increasing annealing duration. This can be attributed to the improvement of

Table 2 Calculating dispersion and oscillator energies using Wemple model for different doping concentrations y $\left[y = \left(\frac{[Zn^{2+}]}{[In^{3+}]} \right)_{sol} = 0, 1, 2, 3, 4, 5 \text{ and } 6 \text{ at.}\% \right]$

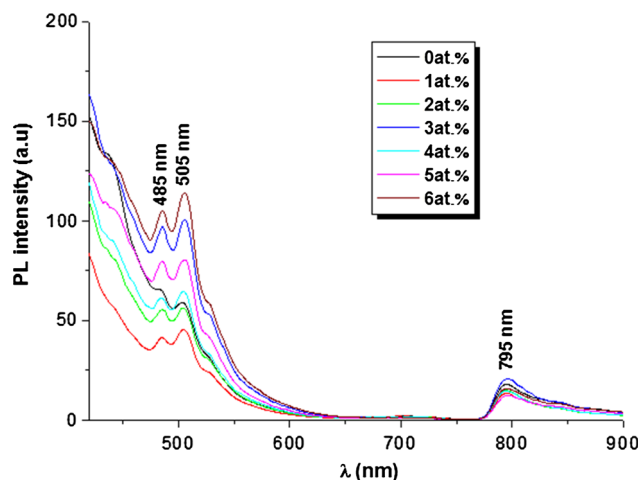| y = [Zn²⁺]/[In³⁺]	E_0(eV)	E_d (eV)	λ_0 (nm)	S_0 ($10^{-5}nm^{-2}$)	
0	5.05	15.02	245.54	4.93	[8]
1	7.45	14.48	166.44	7.01	Present work
2	7.43	13.18	166.89	6.36	
3	7.54	15.05	164.45	7.38	
4	7.32	12.84	169.39	6.11	
5	7.58	17.94	163.58	8.84	
6	7.74	20.11	160.20	10.12	

Fig. 10 Photoluminescence (PL) spectra of undoped and zinc doped In$_2$O$_3$ thin films for different concentrations $\left[y = \left(\frac{[Zn^{2+}]}{[In^{3+}]} \right)_{sol} = 0, 1, 2, 3, 4, 5 \text{ and } 6 \text{ at.\%} \right]$

cristallinity as observed from XRD diffractogramm of as deposited ad annealed layers (Fig. 12) [28]. Indeed, both films annealed at 250 and 450 °C for 2 h were compact and the observed crystallite size are enlarged reducing thus the grain boundaries scattering [29]. This latter is associated with lowering in scattering of light. Nevertheless, a slight decrease of the transmission was detected for films annealed at 450 °C for 1 h. Such result can be due to the decline of the grain size to lower values leading to enlarge of grain boundaries [30] as revealed from Table 4. Pramod et al. [6] have reported that structural defaults and discontinuous grain growth due to lattice mismatch between substrate and crystalline film can be the origin of low transmission values [6]. Generally, it is well known that presence of each of secondary phases, structural defects and considerable roughness (Table 4) lead to a reduction of the transmission [31]. The annealing duration has a considerable impact on structural properties. In fact, for increasing annealing duration, the films exhibit both better

crystallinity and transmission since a rearrangement in the crystal lattice takes place.

Electrical properties were also enhanced by heat treatment. Table 5 shows electrical properties of annealed In$_2$O$_3$:Zn (1 at.%). It is observed a significant decrease of the electrical resistivity by two orders of magnitude from 198.50×10^{-3} to 2.82×10^{-3} Ω cm for respectively undoped and layers annealed at 250 °C during 2 h. At 450 °C and for different annealing durations, a gradual increase of the electrical resistivity is revealed followed by a reduction of the carrier concentration compared with films annealed at 250 °C. A sharp increase of the carrier concentration from 4.70×10^{18} to 2.30×10^{20} cm^{-3} is shown for respectively as grown and films annealed at 250 °C for 2 h. This enhancement of N$_v$ confirms that annealed films becomes highly degenerate (N$_v$ in the order of 10^{20} cm^{-3}). However, Meng et al. [32] have reported that oxygen vacancies caused by the oxygen deficiencies leads to high carrier density. Also, Yuan et al. [4] have explained that the reduction of resistivity after heat treatment may be attributed to an increase of volume carrier concentration. Similar results have been obtained for annealed In$_2$O$_3$ thin films in vacuum. In fact, Yuan et al. [4] have been shown that annealing In$_2$O$_3$ thin films at 500 °C under vacuum for 1 h leads to a decrease of electrical resistivity (1.05×10^{-3} Ω cm) and an increase of the carrier concentration (2.80×10^{20} cm^{-3}).

3.8 Figure of merit

The quality of TCO films is generally affected by optical and electrical properties. To have a relation linking these properties, we have used the Figure of Merit (φ) which correlates between optical transmission (T) and electrical resistivity (ρ). The most used definition of Figure of Merit is given by the following relation [33]:

$$\phi = \frac{T^{10}}{R_s} \qquad (6)$$

Table 3 Electrical parameters of undoped and zinc doped indium oxide thin films as a function of doping ratios $\left[y = \left(\frac{[Zn^{2+}]}{[In^{3+}]} \right)_{sol} = 0, 1, 2, 3, 4, 5 \text{ and } 6 \text{ at.\%} \right]$

$y = [Zn^{2+}]/[In^{3+}]$	Resistivity ($\times 10^{-3}$ Ω cm)	Hall mobility (cm^2/Vs)	Volume carrier concentration ($\times 10^{18}$ cm^{-3})
0	650.20	1.17	8
1	198.50	6.70	4.70
2	4014	0.98	1.57
3	8801	4.28	0.17
4	1572	0.64	6.24
5	3431	0.18	10.20
6	4260	6.12	0.24
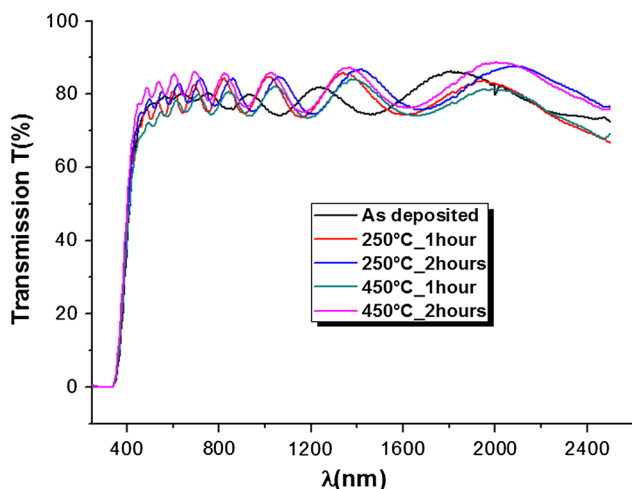
Fig. 11 Transmission spectra of heated In$_2$O$_3$:Zn (1 at.%) for different annealing conditions

Table 4 Grain sizes and RMS roughness of In$_2$O$_3$:Zn (1 at.%) for different annealing conditions

Annealing conditions	Grain size (nm)	RMS roughness (nm)
As deposited	94	59
250 °C, 1 h	70	87
250 °C, 2 h	103	55.4
450 °C, 1 h	82	73
450 °C, 2 h	121	35.2

Table 5 Electrical parameters of as deposited and annealed In$_2$O$_3$:Zn (1 at.%) at different temperatures and durations

Annealing temperatures	Resistivity ($\times 10^{-3}$ Ω cm)	Hall mobility (cm^2/Vs)	Volume carrier concentration ($\times 10^{18}$ cm^{-3})
As deposited	198.50	6.70	4.70
250 °C, 1 h	33.46	0.93	201
250 °C, 2 h	2.82	0.96	230
450 °C, 1 h	96.59	1.07	60.50
450 °C, 2 h	13.68	0.48	95.90

Fig. 12 XRD patterns of In$_2$O$_3$:Zn (1 at.%) annealed at different conditions
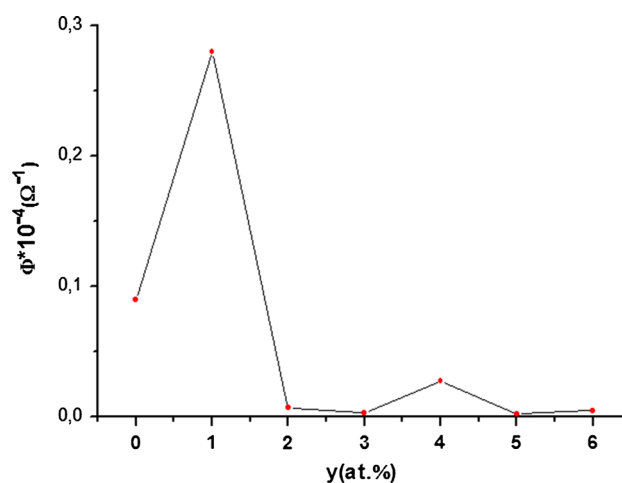

Fig. 13 Figure of Merit (Φ) of zinc doped indium oxide thin films for different atomic concentrations y (y = 0, 1, 2, 3, 4, 5 and 6 at.%)

where T is the average transmission. R$_s$ is the sheet resistance which is calculated using:

$$R_s = \frac{\rho}{t} \tag{7}$$

The Figure of Merit ϕ of In$_2$O$_3$ thin films versus zinc doping concentration y are shown in Fig. 13. After doping,

ϕ increases from 0.09×10^{-4} to 0.28×10^{-4} Ω^{-1} for respectively undoped and In$_2$O$_3$:Zn (1 at.%). Beyond y equals to 1 at.%, ϕ decreases significantly reaching a minimum value of 0.0023×10^{-4} Ω^{-1}. This result may be a consequence of the increase of resistivity by an order of magnitude for y greater than 1 at.%. The greater value of ϕ is obtained for In$_2$O$_3$:Zn (1 at.%) which correspond to the best crystalline quality films as shown in Fig. 1.

Figure 14 exhibits the Figure of Merit ϕ as function of annealing conditions annealing for y equals to 1 at.%. The
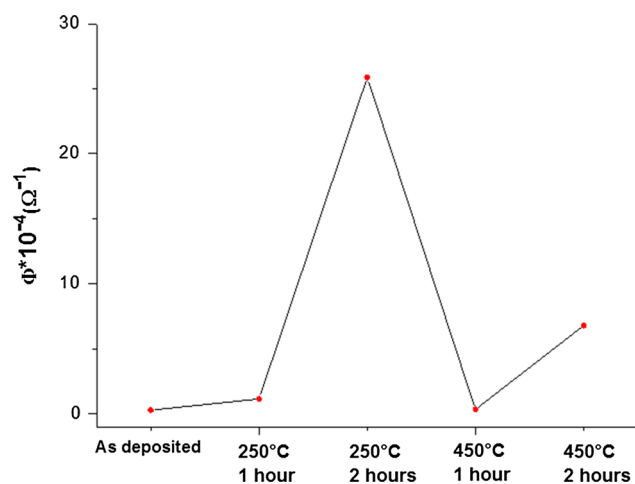
Fig. 14 Figure of Merit (Φ) of In_2O_3:Zn (1 at.%) as a function of annealing temperatures and for different durations

Figure of Merit of annealed thin layers is greater than as deposited one. This result leads to confirm that the heat treatment process enhances the quality of elaborated TCO layers. In fact, ϕ increases sharply from 0.28×10^{-4} to $24.86 \times 10^{-4} \ \Omega^{-1}$ for respectively as deposited and films annealed at 250 °C during 2 h. This result may be due to the significant decrease of the resistivity and enhance of transmission after annealing. Hence, In_2O_3:Zn (1 at.%) thin films heated at 250 °C for 2 h are the most promising TCO among our elaborated In_2O_3 thin layers.

4 Conclusion

Zinc doped indium oxide thin films have been prepared using spray pyrolysis. XRD analysis show that preferred orientation is changed after doping from (222) to (400). The well crystallized In_2O_3:Zn were obtained for y equals to 1 at.%. The grain size was found to be maximum for In_2O_3:Zn (1 at.%) thin films reaching 93.4 nm. The maximum value of RMS roughness was obtained at this doping level. After doping a slight decrease in the transmission was observed but approximately all films are highly transparent (T in the order of 80 %). An increase of band gap energy was noted after doping up to 4 at.% reaching the theoretical of TCO band gap material (3.5 eV). A minimum of electrical resistivity in the order of $198.50 \times 10^{-3} \ \Omega$ cm was obtained for y equals to 1 at.%. A further decrease of resistivity, accompanied with an increase of transmission, is founded after heat treatment at 250 °C reaching a minimum value of $2.82 \times 10^{-3} \ \Omega$ cm. Finally, the physical properties of In_2O_3 thin films are globally enhanced by zinc doping and heat treatment process. All these experimental results leads to conclude that

annealed In_2O_3:Zn (1 at.%) can be used as TCO material in optoelectronic devices.

References

1. C. Manoharan, M. Jothibas, S.J. Jeyakumar, S. Dhanapandian, Spectrochim. Acta Part A Mol. Biomol. Spectrosc. **145**, 47–53 (2015)
2. L.N. Lau, N.B. Ibrahim, H. Baqiah, Appl. Surf. Sci. **345**, 355–359 (2015)
3. M.A.M. Khan, W. Khan, M. Ahamed, M. Alhoshan, Mater. Lett. **79**, 119–121 (2012)
4. Z. Yuan, X. Zhu, X. Wang, X. Cai, B. Zhang, D. Qiu, H. Wu, Thin Solid Films **519**, 3254–3258 (2011)
5. Y.H. Shin, S.B. Kang, S. Lee, J.J. Kim, H.K. Kim, Org. Electron. **14**, 926–933 (2013)
6. N.G. Pramod, S.N. Pandey, Ceram. Int. **41**, 527–532 (2015)
7. V.S. Vaishnav, S.G. Patel, J.N. Panchal, Sens.Actuators B **206**, 381–388 (2015)
8. N. Beji, M. Souli, M. Ajili, S. Azzaza, S. Alleg, N. Kamoun, Turki. Superlattices Microstruct. **81**, 114–128 (2015)
9. H. Baqiah, N.B. Ibrahim, M.H. Abdi, S.A. Halim, J. Alloys Compd. **575**, 198–206 (2013)
10. A.H. Ali, A. Shuhaimi, Z. Hassan, Appl. Surf. Sci. **288**, 599–603 (2014)
11. M. Cesaria, A.P. Caricato, G. Maruccio, M. Martino, J. Lumin. **162**, 155–163 (2015)
12. M. Jothibas, C. Manoharan, S. Ramalingam, S. Dhanapandian, M. Bououdina, Spectrochim. Acta Part A Mol. Biomol. Spectrosc. **122**, 171–178 (2014)
13. S. Louidi, F.Z. Bentayeb, W. Tebib, J.J. Suñol, A.M. Mercier, J.M. Grenèche, J. Non-Cryst. Solids **356**, 1052–1056 (2010)
14. M. Ajili, M. Castagné, N. Kamoun, Turki. Superlattices Microstruct. **53**, 213–222 (2013)
15. S. Parthiban, V. Gokulakrishnan, K. Ramamurthi, E. Elangovan, R. Martins, E. Fortunato, R. Ganesan, Sol. Energy Mater. Sol. Cells **93**, 92–97 (2009)
16. S. Parthiban, E. Elangovan, K. Ramamurthi, R. Martins, E. Fortunato, Sol. Energy Mater. Sol. Cells **94**, 406–412 (2010)
17. S. Kaleemulla, N.M. Rao, M.G. Joshi, A.S. Reddy, S. Uthanna, P.S. Reddy, J. Alloys Compd. **504**, 351–356 (2010)
18. Y.-R. Lyu, T.-E. Hsieh, Surf. Coat. Technol. **231**, 219–223 (2013)
19. M. Reghima, A. Akkari, C. Guasch, N. Kamoun, J. Renew. Sustain. Energy **7**, 023128 (2015)
20. J. Liu, D. Wu, S. Zeng, J. Mater. Process. Technol. **209**, 3943–3948 (2009)
21. S. Cho, Microelectron. Eng. **89**, 84–88 (2012)
22. D. Beena, K.J. Lethy, R. Vinodkumar, V.P.M. Pillai, V. Ganesan, D.M. Phase, S.K. Sudheer, Appl. Surf. Sci. **255**, 8334–8342 (2009)
23. S. Belgacem, R. Bennaceur, Revue. Phys. Appl. **25**, 1245–1258 (1990)
24. H. Khallaf, G. Chai, O. Lupan, L. Chow, H. Heinrich, S. Park, A. Schulte, Phys. Status Solidi A **206**(2), 256–262 (2009)
25. V. Senthilkumar, P. Vickraman, M. Jayachandran, C. Sanjeeviraj, Vacuum **84**, 864–869 (2010)
26. S. Kaleemulla, A.S. Reddy, S. Uthanna, P.S. Reddy, Optoelectron. Adv. Mater. Rapid Commun. **2**(12), 782–787 (2008)

27. P. Wu, Q. Li, C.X. Zhao, D.L. Zhang, L.F. Chi, T. Xiao, Appl. Surf. Sci. **255**, 3201–3204 (2008)
28. V. Senthilkumar, P. Vickraman, Curr. Appl. Phys. **10**, 880–885 (2010)
29. J. Lee, Y.S. Park, Thin Solid Films **587**, 94–99 (2015)
30. J. Sengupta, A. Ahmed, R. Labar, Mater. Lett. **109**(15), 265–268 (2013)

31. B.P. Kafle, S. Acharya, S. Thapa, S. Poudel, Ceram. Int. **42**, 1133–1139 (2016)
32. F. Meng, J. Shi, Z. Li, Y. Cui, Z. Lu, Z. Feng, Sol. Energy Mater. Sol. Cells **122**, 70–74 (2014)
33. A.V. Moholkar, S.M. Pawar, K.Y. Rajpure, V. Ganesan, C.H. Bhosale, J. Alloys Compd. **464**, 387–392 (2008)